

# 3D MEASUREMENTS TO DETERMINE MICROMECHANICAL ENERGY DISSIPATION IN STEEL FIBER REINFORCED CONCRETE

KEVIN J. TRAINOR, LAUREN S. FLANDERS AND ERIC N. LANDIS

University of Maine  
Department of Civil & Environmental Engineering  
Orono, Maine 04469, USA  
e-mail: landis@maine.edu

**Key words:** Fracture, Damage, Fiber reinforced cement composites, x-ray tomography

**Abstract.** Adding sufficient quantities of steel fibers to concrete has long been known to transition a relatively brittle material to a relatively ductile one. That transition is made possible by a number of well known toughening mechanisms including, fiber-matrix debonding and pull-out, additional matrix cracking, as well as fiber bending and fracture. In the work here, we seek to measure these different energy dissipation mechanisms through the analysis of 3D microstructural images. Reinforced and unreinforced flexure specimens of ultra high performance concrete were scanned using an x-ray computed tomography (CT) imaging system that allowed quantitative measurement and characterization of internal features. The CT imaging was done in conjunction with three point bending tests of notched specimens. Unreinforced specimens were used to measure specific fracture energy in a way that accounts for the irregular shape of the fracture surface. For fiber-reinforced specimens, 3D digital image analysis techniques were used to measure fiber volume fraction, as well as the orientation of individual fibers. In post-fracture scans, the total amount of internal cracking was measured, as was the degree of fiber pullout relative to undamaged specimens. Measurements show that with a nominal steel fiber volume fraction between 3.5 and 4.0%, there is a hundred-fold increase in energy dissipated. Through quantitative analysis of the tomographic images, we could account for roughly 90% of this increase. The analysis shows that roughly half of the internal energy dissipation comes from matrix cracking, including the crack branching and multiple crack systems facilitated by the fibers, while the remaining energy dissipation is due to fiber pull-out.

## 1 INTRODUCTION

The technological significance of reinforcing cement-based composites with steel fibers is well established and well documented (e.g. [1, 2]). The presence of fibers can convert the brittle matrix to a toughened high performance composite. The mechanisms that facilitate this transition are well established: matrix toughening through multiple cracking, fiber pullout, and fiber deformation fracture, and others. The evidence pointing to the role of these mechanisms is substantial. What is not documented as

well, however, are quantitative measurements that isolate the relative contributions of the different toughening mechanisms. That is, we can easily measure the overall increase in the work of load required to deform a fiber-reinforced specimen compared to an unreinforced specimen, but it is much more difficult to quantify the relative contributions to this increase by the different toughening mechanisms.

In the work described in this paper, we combine simple laboratory mechanical testing with advanced 3D imaging and image analysis to

isolate and measure the relative contributions of different micromechanical phenomena to the overall increase in the energy dissipation capacity of the material. We focus on a particular combination of high strength reactive powder concrete with hooked steel fibers. Reactive powder concrete is quite brittle due to its relatively homogeneous microstructure (as compared with conventional portland cement concrete), and as such, the addition of a relatively high volume fraction of steel fibers lead to orders of magnitude increase in overall toughness.

The motivation for this work is to quantify the energy associated with different micromechanical phenomena so that we have a more fundamental basis for numerical material models. The assumption being that if we can better capture the micromechanical mechanisms, our models will be more universal and less dependent on different calibrations for different geometric or loading conditions.

## 2 MATERIALS

The specimens used in this study were plain and reinforced reactive powder concrete. Reactive powder concretes are high performance cement-based materials with low water to cement ratios, high cement paste contents, and no coarse aggregate particles [3]. “Aggregates” consist of a fine (0.6 mm maximum nominal diameter) silica sand and fine silica flour. Cementitious materials are type H portland cement and silica fume. Because of the low water-cement ratios, high range water reducing admixtures are required for proper workability.

The specimens used in this study were proportioned according to the quantities listed in Table 1, and according to the details provided in Williams et al [4]. Freshly cast specimens were placed in an environmental chamber held at 22°C and 100% RH. After 7 days, specimens were submerged in an 85°C bath for four days, and then oven dried at 85°C for 2 days. The material had a nominal compressive strength of 200 MPa.

**Table 1:** Table of Concrete Matrix Constituents

Constituent	% by mass
Cement	35.0
Sand	33.8
Silica Flour	9.7
Silica Fume	13.6
Superplasticizer	0.6
Water	7.3

Some of the specimens were reinforced with nominally 3.6% steel fibers by volume. The steel fibers were 30 mm long and 0.55 mm diameter. The ends of the fibers were deformed to improve pull-out capacity. The manufacturer (Dramix) specifies an elastic modulus of 200 GPa and a tensile strength of 1100 MPa. Fibers were added to the fresh concrete after it reached a flowable consistency. Fibers were dispersed by continued mixing of the material.

The plain and reinforced beam specimens used in this study were cast with nominal dimensions of 220 by 48 by 30 mm, length, depth, and width, respectively. After curing, a 5 mm wide by 18 mm deep saw cut was made at the midspan.

## 3 Experiments

### 3.1 Three Point Bending Tests

All specimens considered here were subjected to three-point bending tests using the experimental configuration illustrated in Fig. 1. Unreinforced specimens were tested using crack mouth opening displacement (CMOD) control to ensure stable crack growth. Load was applied such that CMOD opened at a rate of 0.15 mm/min. Because of the stable crack configuration, specimens could be loaded until the load on the specimen was nearly zero and the crack propagated nearly the entire depth of the specimen. For this work, tests were completed when the load on the specimen dropped below 1% of the maximum. For reinforced specimens, stable crack growth was not an issue, as all specimens exhibited highly ductile behavior. As such, the specimens were tested using position (stroke) control, at a deformation rate of

0.15 mm/min. The test ran until the load on the specimen was approximately 50% of the maximum. Midspan deformation was measured by a pair of LVDT displacement gages mounted to the three-point bend fixture. The test fixture was sufficiently stiff so that deformation of supports did not cause more than 1% error in the deformation measurement.

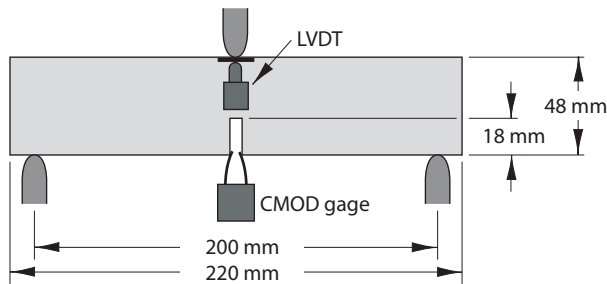


Figure 1: Schematic illustration test configuration.

Example load-deformation plots for unreinforced and reinforced specimens are shown in Fig. 2. Note the difference in the load-deformation responses of the two specimen types. The reinforced specimen has eight times the load and ten times the deformation, as compared to the unreinforced specimen.

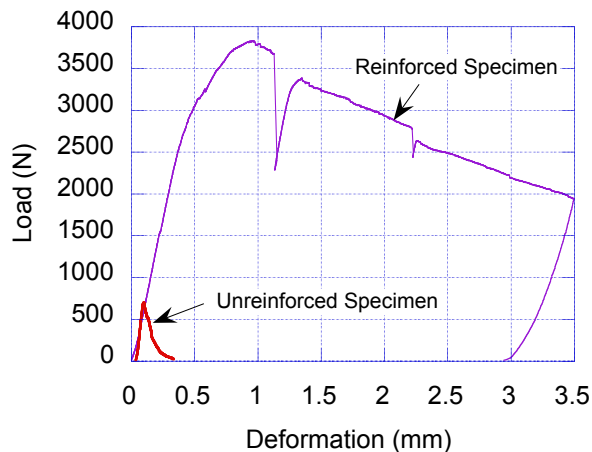


Figure 2: Example load-midspan deflection plot for unreinforced and reinforced specimens.

For both specimen types, the work of load was determined by calculating the area under

the load-deformation plots. In the case of the reinforced specimens, all of which still carried significant loads at the end of testing, the area under the unloading portion of the curve is subtracted, leading to what is referred to here as net work of load,  $W_{ext}$ , as illustrated in Fig. 3. In the case of the unreinforced and reinforced specimens whose plots are shown in Fig. 2, the reinforced specimen has nearly 120 times greater net work of load.

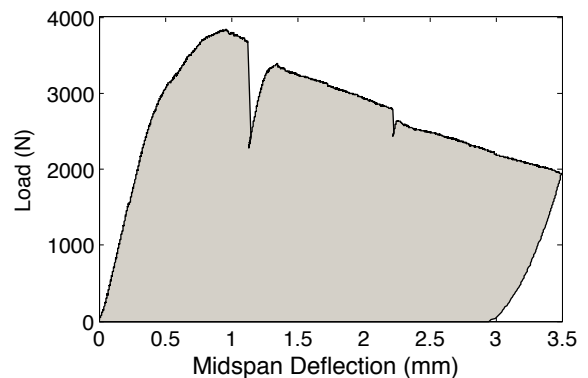


Figure 3: Illustration of net work of load calculation based on load-deflection data.

### 3.2 X-ray Computed Tomography

The internal structure of the specimens tested was evaluated by exploiting 3D x-ray computed tomographic (CT) imaging. CT images are 3D maps of x-ray absorption in a material. The imaging is accomplished by making multiple x-ray radiographs of a specimen at different angles. A tomographic reconstruction manipulates the 2D radiographs in such a way to produce a complete 3D image of the specimen's internal structure. Internal features such as pores, cracks, and fibers can be precisely located inside the specimen. X-ray CT techniques have been applied to concrete by a number of researchers [5, 6] because of its versatility in spatial imaging.

In this work, tomographic scans were made with an industrial scale CT system consisting of a microfocus x-ray source operating at 120kV and  $0.875 \mu\text{A}$ . X-rays were passed through a 1.25 mm copper filter to remove lower energy

components, thereby reducing beam-hardening artifacts. During tomographic scans, 720 projection radiographs were captured by a 2000 x 2000 pixel detector at 0.5° angle increments over a complete 360° rotation. A complete tomographic scan took approximately 110 minutes. Tomographic reconstruction was done using a proprietary algorithm produced by the instrument vendor (Northstar Imaging, Inc.). The reconstruction process produced a 3D image volume of 2000 x 2000 x 2000 voxels covering a volume of 60 x 60 x 60 mm, with each voxel being a 30  $\mu\text{m}$  cube. Example raw and processed tomographic images are shown in Fig. 4. In these images, brightness is proportional to x-ray absorption, so highly absorptive steel fibers are light, while voids and cracks are dark. It should be emphasized that since Fig. 4(a) just shows a single slice, overall fiber morphology is not necessarily visible. What is shown is the intersection of fibers with the particular 2D plane. The 3D rendering of Fig. 4(b) better illustrates fiber orientation and morphology due to the partial transparency of the surrounding concrete matrix.

Because the beams have a high aspect ratio relative to the geometry of the CT scanner used in this work, only the middle third of the beam was scanned. The nature of localized damage induced in the three-point bending configuration gave reasonable assurance that no cracking occurred outside the region scanned.

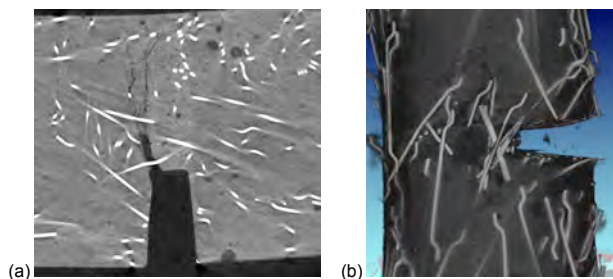


Figure 4: Example segments of tomographic reconstruction: (a) slice image (b) 3D rendering with partial transparency.

## 4 3D Image Processing

Images such as those shown in Fig. 4 are valuable for providing a qualitative picture of a material's internal structure, but the digital nature of the image data allows us to make numerous quantitative measurements as well. In this section, we detail several techniques used to quantify internal structure, and how we can use that information to deduce relative magnitudes of energy dissipation.

### 4.1 Fracture Surfaces of Unreinforced Concrete

The first step in our image analysis was to measure the fracture surface area of the unreinforced specimens. In this work, we applied an approach that allowed us to consider the irregular and non-euclidean nature of fracture surfaces by exploiting the 3D imaging capabilities of x-ray CT. Specifically, we can isolate the fracture surface by first segmenting the images to separate solid from void or air. From this segmented image, the surface of the specimen can be identified, as shown in Fig. 5(a). The fracture surface is removed from the rest of the specimen boundary through a 3D "cropping" as illustrated in Fig. 5(b). The surface area is determined by adding up all the voxel faces that make up the surface for both crack faces.

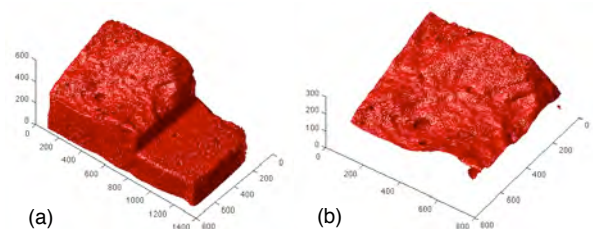


Figure 5: 3D rendering of fracture surface of unreinforced specimen (a), and extracted fracture surface (b).

As discussed in more detail below, this surface area measurement is used to determine the energy dissipated by cracking in the fiber reinforced specimens.

## 4.2 Fiber Volume Fraction

As previously noted and illustrated in Fig. 4, the highly absorptive nature of the fibers relative to the concrete matrix means that digital separation or segmentation can easily be accomplished based on voxel brightness. Specifically, a threshold value is chosen so that any voxel that has a brightness greater than or equal to the threshold is considered part of a fiber, while any voxel below the threshold is considered to be concrete or air. It should be noted that varying this threshold value can lead to different numbers of fiber voxels. In order to set a correct threshold value, the diameters of fibers isolated in the 3D image were compared to the true fiber diameter of 0.55 mm. The threshold value was established so that the average image-based fiber diameter was also 0.55 mm.

**Table 2:** Table of Typical Reinforced Beam Properties

Beam	$V_f(\%)$	$P_{max}$ (N)	$W_{ext}$ (mJ)
1	3.54	3832	10480
2	3.46	3686	14240
3	4.16	3479	7080
4	3.77	2343	7300
5	3.99	4186	14580
6	4.03	3911	11600

Table 2 shows sample values of fiber volume fraction along with the corresponding peak load and net work of load. Of note is the fact that these fiber volume fractions are comparable with that dictated by the mix design. This indicates that although only the central section of the beams was scanned, the volume scanned was representative of the entire specimen volume. Also of interest in the table is the relationship between fiber volume fraction and both peak load and net work of load. While one might expect the fiber volume fraction to affect both, the table shows no relationship within the range of the fiber volume fraction tested. As shown below however, the *orientation* of the fibers has a pronounced affect.

## 4.3 Analysis of Fiber Orientation

The orientation of reinforcement dictates the performance of the composite to a significant degree. For this analysis, a method based on the work of Krause et al. [7], Lorenz [8], and Nagel [9] was used to find the orientation of reinforcement at every voxel comprising the fibrous reinforcement. The method is based on the Hessian matrix, a square second order tensor containing the partial derivatives of a function measuring the local curvature. Use of the Hessian matrix depends on the assumption that the 3D digital volume represents the discretized version of a continuous, twice differentiable 3D function [7].

In this study, the Hessian analysis was conducted on a twice lowpass filtered volume. The initial filtering with a block kernel smooths the fiber surfaces, and subsequent filtering with a Gaussian kernel smooths the local peaks in intensity at fibers. Initial filtering reduces the effects of noise on the second derivatives in the Hessian [9]. After lowpass filtering was complete, the Hessian,  $H(I)$ , was formulated from the image intensity at each fiber point. Specifically:

$$H(I) = \begin{pmatrix} \frac{\partial^2 I}{\partial x^2} & \frac{\partial^2 I}{\partial x \partial y} & \frac{\partial^2 I}{\partial x \partial z} \\ \frac{\partial^2 I}{\partial y \partial x} & \frac{\partial^2 I}{\partial y^2} & \frac{\partial^2 I}{\partial y \partial z} \\ \frac{\partial^2 I}{\partial z \partial x} & \frac{\partial^2 I}{\partial z \partial y} & \frac{\partial^2 I}{\partial z^2} \end{pmatrix}, \quad (1)$$

where  $I$  is the voxel intensity at point  $(x, y, z)$ . The fiber orientation at that point is defined by the eigenvector of  $H(I)$  corresponding to the third eigenvalue. This vector indicates the direction in which there is the least variation in intensity; acceptance of this as the fiber orientation is based on the observation that the transverse axes of a fiber will have highly negative second derivatives due to the peak in intensity, while moving along the longitudinal axis will not produce a substantial change in intensity [8]. Fig. 6 illustrates the orientation vectors generated for a set of fibers using this method.

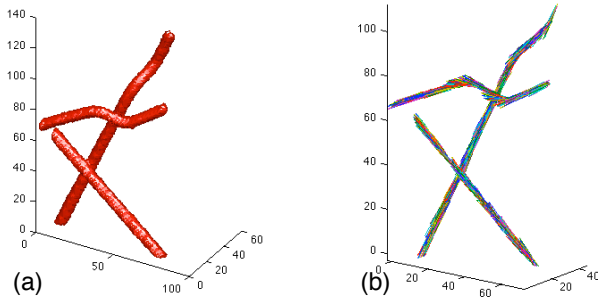


Figure 6: 3D rendering of isolated fiber segments (a), with corresponding vector representation (b).

The fiber orientation is critical to material performance. Fig. 7 shows fiber angle distributions for three different beam specimens of varying fiber volume fraction,  $V_f$ , strength,  $P_{max}$ , and bulk energy absorption (labeled as net work of load,  $W_{ext}$ ). All three specimens shown have a reasonably similar fiber volume fraction; however, they each have a very different peak load and net work of load. The basis for these differences can be seen in the orientation distribution. While all three have a fiber angle mode of about  $22^\circ$ , Beam 4 has a much higher fraction of fibers oriented at higher angles. In the limit cases, a fiber with an angle approaching  $0^\circ$  would be most efficient, while a fiber at  $90^\circ$  would provide no reinforcement. Indeed, fibers oriented transversely to the direction of maximum stress can even act as a pathway to facilitate crack growth, weakening the specimen. Thus, the specimen with the highest concentration of fibers oriented between  $0$  and  $40^\circ$  (Beam 5) also has the highest peak load and the highest bulk energy absorption. Beam 2 has high energy absorption, but a 12% lower peak load due perhaps to a cluster of transversely oriented fibers. Beam 4 is the weakest and has the lowest energy absorption due to the fewest number of fibers aligned with the specimen axis.

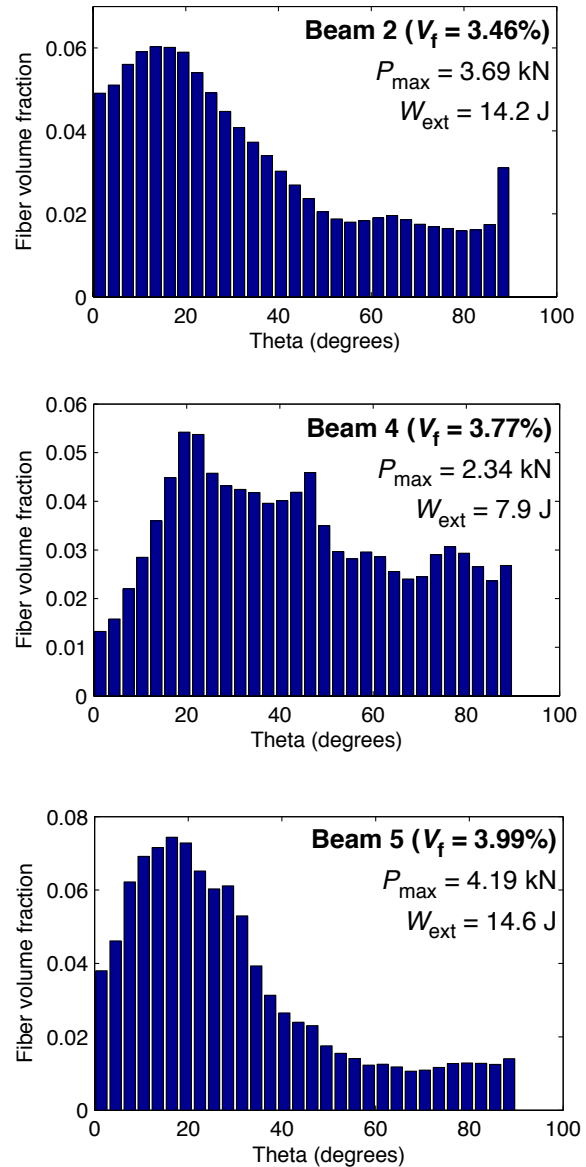


Figure 7: Histograms of fiber orientation in three different specimens. Fiber angle, theta, is measured from the fiber axis to the longitudinal axis of the beam.

#### 4.4 Measurement of Fiber Debonding and Pull-out

As fiber pull-out is an important toughening mechanism for fiber reinforced composites, great care was taken in this work to measure its effects on overall toughness. In this study, the extent of fiber pullout was measured manually by visually identifying fibers displaying pullout and then measuring the distance of pullout using the digital image. Fig. 8(a) shows an exam-

ple of fiber pullout as seen in a 2D slice image.

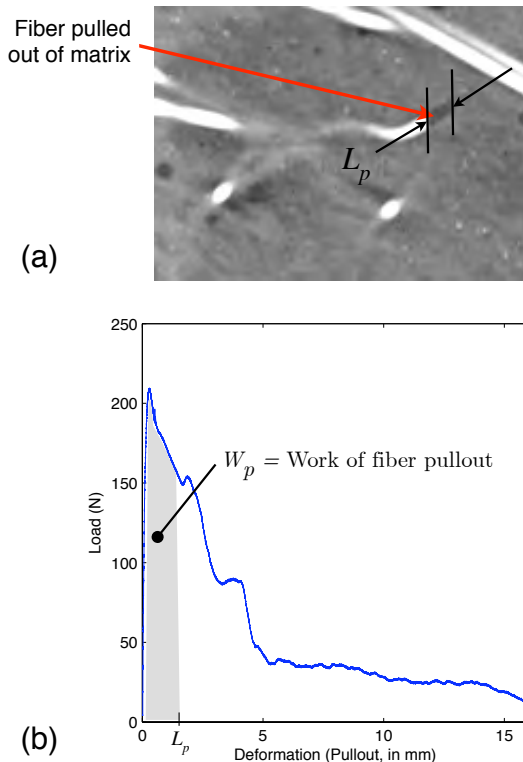


Figure 8: Example slice segment showing fiber pulled out from matrix.

In order to estimate the work required to achieve the measured fiber pull-out, we turned to data produced at the U.S. Army Engineer Research and Development Center (ERDC) [10], where force versus pull-out length was measured for the same fiber-matrix combination as used here (shown in Fig. 8(b)). The work of fiber pull-out was determined by taking the area under the force versus pull-out curve up to the length of pull-out measured in the CT images. This was done for each fiber for which pull-out was measurable.

We should note that there are several issues that arise using pull-out tests to estimate in situ pull-out work. First is the quality of the pull-out data. The pull-out tests were quite repeatable due to the high quality of the cement matrix. Indeed, the locations of the “bumps” in the descending portion of the curve corresponded to the bending of the fiber hooks during pull-

out, and these bumps were consistent. The second issue is the angle of fiber pull-out. In the pull-out tests, the load axis was aligned with the fiber axis; however, this is not necessarily the case for the fibers imbedded in the beam specimens. Regardless, we believe this to be a reasonable approximation because, while the force required for pull-out will change with pull-out angle, only the force component parallel to the fiber is actually doing work. The assumption made here is that as long as the movement perpendicular to the fiber axis is small, then the damage in that direction is small, and the pull-out data is a reasonable proxy. This is further supported by the observation that fibers with measurable pull-out did not typically have large angles relative to the specimen axis.

#### 4.5 Crack Area in Reinforced Specimens

As described above, analysis of CT images allows us to measure crack area in a way that reasonably accounts for all the irregular, tortuous surfaces that make up the crack. In the unreinforced material, this was simplified because of the single crack that resulted from notched beam fracture. In the reinforced specimens, the crack surfaces become much more interesting because the fiber crack bridging allows a large network of branching cracks to develop. Thus the energy dissipated by matrix cracking can jump considerably over that of the unreinforced specimens.

Isolation of the crack network was not as straightforward as one would think. The presence of the highly absorptive steel fibers in the material shifts the x-ray absorption profile in such a way that small cracks are difficult to isolate from the matrix. That is, if one considers a histogram of voxel intensities in the images, the less absorptive concrete matrix and the void space form a very narrow intensity range compared to the much “brighter” steel fibers. Thus, for this study, cracks were manually identified slice by slice as illustrated in Fig. 9. Once the cracks are traced, they can easily become labeled objects in the image that can then be isolated and measured in the same way as the crack

area in the unreinforced specimens described above.

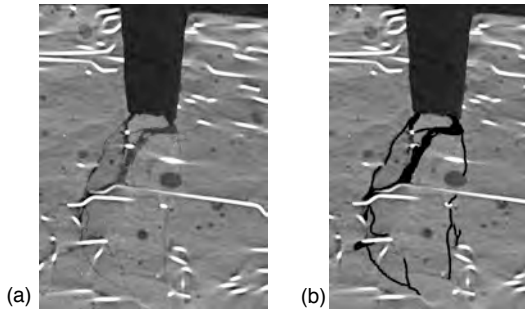


Figure 9: Illustration of crack tracing in a particular slice image. (a) shows original slice image, and (b) shows same image after crack network has been mapped.

#### 4.6 Other Energy Dissipation Mechanisms

Two other energy dissipation mechanisms were considered; both involve fibers bridging cracks. The first involved bending of fibers that cross cracks. As illustrated in Fig. 10, the discontinuity of the crack can, in some instances, cause a kinking of the fiber. This kinking requires a certain amount of work to form the plastic hinges that make up the kinks. Using the fiber angle measurement techniques described above, the angle of individual fiber kinks can be measured and used to calculate the work required to form a plastic hinge. This work is simply the kink angle multiplied by the fiber’s plastic moment, which was determined from the fiber yield stress and moment of inertia.

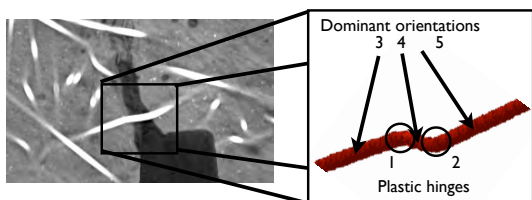


Figure 10: Measurement of plastic hinge formation in steel fibers.

The second additional energy dissipation mechanism is an extension of the fiber pull-out. However, in this case it is an indirect measurement. Specifically, we frequently observe fibers that bridge cracks yet have no measurable pull-out from the matrix at the fiber ends. For these fibers, continuity dictates that some slippage along the interface must have occurred unless the fibers measurably elongated, which was not observed. This “bridging energy” was determined by first identifying all fibers that intersected the crack network, but did not exhibit measurable pull-out at the ends. For these fibers, a pull-out work was calculated by taking the area under the pull-out test curve of Fig. 8(b) up to the distance of crack opening at the fiber bridging point.

## 5 Results and Discussion

The image processing techniques described in the previous section allow us to make measurements of internal changes in material structure during damage. In this work we seek to translate those changes into quantifiable energy dissipation mechanisms, which can be summed and compared to the energy dissipated by the entire specimen during loading.

### 5.1 Matrix Fracture Energy

The energy dissipated by crack growth in the concrete matrix was determined from the three point bend tests of unreinforced specimens. This was calculated by dividing the net work of load (as illustrated for a reinforced specimen in Fig. 3) by the crack surface area, measured as described above. That is, the specific energy of fracture,  $G_f$  is calculated by:

$$G_f = \frac{U_{ext}}{\Delta A}, \quad (2)$$

where  $\Delta A$  is the newly created surface area in the fractured material, and  $U_{ext}$  is the total consumed energy, determined by recognizing that the net work of load must be equal to the energy consumed by the specimen:

$$U_{ext} = W_{ext}. \quad (3)$$

For the concrete matrix material used here, using Eq. (2), we determined a mean specific fracture energy of  $24\text{J}/\text{m}^2$  with a COV of 16%.

## 5.2 Energy Balance

The focus of this work was to quantify the different micromechanical toughening mechanisms that lead to the overall increase in toughness for the bulk material. Given the 3D image processing tools for fiber pull-out, fiber bending, and fiber bridging, described in the previous section, we are in a position to do just that.

If we denote the work of fiber pull-out, fiber bending, and fiber bridging as  $W_p$ ,  $W_b$ ,  $W_r$ , respectively, we may calculate the total internal energy dissipation,  $U_{int}$  as:

$$U_{int} = W_f + W_p + W_b + W_r \quad (4)$$

where  $W_f$  is the energy of concrete matrix cracking, determined simply by taking the specific fracture energy defined in Eq. (2), and multiplying it by the area of measured matrix cracking,  $\Delta A$ :

$$W_f = G_f \cdot \Delta A \quad (5)$$

The total internal energy calculation of Eq. (4) was carried out for three specimens and is presented in Table 3. Also shown in the table is a fractional comparison of the total internal energy dissipation to the external work of load, which was included in Table 2. The measurements show some variation between different energy dissipation mechanisms. In all cases, fiber pullout dissipated the greatest energy, followed by either matrix cracking or fiber bridging. Also in all cases, fiber bending has a very small contribution.

Additionally, it is immediately seen that the measured internal energy dissipation is only between two thirds and three quarters of the net measured work of load. Clearly there are significant energy dissipation mechanisms that are not accounted for in this analysis.

Table 3: Internal Energy Dissipation Totals (Energy Units of mJ)

Beam	$W_f$	$W_p$	$W_b$	$W_r$	$E_{int}$	$\frac{U_{int}}{U_{ext}}$
4	1250	2020	130	1950	5350	73%
5	3500	4720	190	1000	9410	65%
6	2210	3890	180	2270	8550	74%

## 5.3 Additional Energy Dissipation

The nature of failure in the reinforced beams tested leads to some obvious and some less obvious additional sources of energy dissipation in the specimens. For many of the specimens, there were fragments that either spalled off the surface of the specimen or fell out of the interior of the specimen. Every effort was made to contain these pieces that completely disconnected from the specimen, but occasionally fragments were lost. In these cases, only half of the generated crack area was measured in our analysis.

A less obvious source of energy dissipation comes from consideration of additional matrix cracking. The absolute maximum spatial resolution of the 3D images is the voxel size of  $30\ \mu\text{m}$ . However, in images such as these, where microstructural variations occur at a scale finer than the voxel size, an object of interest really needs to be several voxels wide for robust detection. In this work, crack identification required the crack to be at least 3 voxels wide; at the resolution used in manual crack identification, this is 0.01 mm. Thus, any crack with an opening smaller than 0.01 mm is not visible in the CT images. In order to estimate the extent of cracking not visible in the CT images, optical microscope images with a nominal resolution of  $4\ \mu\text{m}$  were taken of fractured reinforced specimens. These images revealed a large network of cracks below the observable threshold, as shown in Fig. 11, where cracks visible in the CT images are labeled “visible cracks,” and those not seen in the CT images are labeled “invisible cracks.” While a direct comparison can only be made on the surface of the specimen, measurements showed that at the higher resolution the length of the crack network doubled. Assuming this phenomenon exists throughout

the specimen, we estimate the measured energy of matrix cracking is nominally half of the actual energy of matrix cracking. If we double the energy of matrix cracking, then the  $G_f$  values of Table 3 become 2500, 7000, and 4420 mJ for Beams 4, 5, and 6, respectively. It should be noted that undamaged specimens were also examined to be sure that surface cracks were in fact due to damage as opposed to shrinkage cracking. Thus, implicit in the analysis here is that all measured matrix cracking is induced by the work of the load, as opposed to shrinkage or other mechanisms.

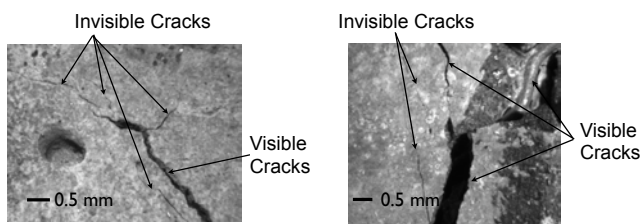


Figure 11: Micrographs of cracks on specimen surface. The images illustrate the limitations of X-ray CT resolution, as cracks seen under microscope are not visible in CT images.

#### 5.4 Analysis of Toughening Mechanisms

With these new values of matrix cracking, new totals for the distribution of internal energy dissipation is presented in Table 4. While the internal totals still do not quite add up to the overall net external work of load, the totals are close enough to be considered a reasonable accounting.

It is interesting to note the relative contribution of different toughening mechanisms to overall material toughness, as revealed in Table 4. In all cases, matrix cracking dissipates the greatest amount of energy, followed in each case by fiber pullout. This is particularly interesting, because it further confirms a case made by Shah [11] that fibers have the effect of toughening the matrix without actually modifying the fracture energy of the matrix. This is because the fibers force branching of matrix cracks so that a relatively brittle matrix material has the

capacity to dissipate considerably more energy. The data presented here show that the inclusion of fibers increases the matrix crack area between 27 (Beam 4) and 75 times (Beam 5). Thus, we have changed a brittle matrix with limited ability to dissipate energy, to one that provides the highest relative contribution to internal energy dissipation.

## 6 Conclusions

The results of this work show how internal energy dissipation mechanisms in a fiber reinforced high performance cement-based composite can, to a certain degree, be measured by combining standard mechanical testing with the 3D imaging capabilities of x-ray computed tomography. Quantitative analysis of the 3D CT images allowed us to measure the distribution and orientation of hooked steel fibers embedded in the high strength concrete matrix. In addition, changes in physical structure: cracking, fiber bending, fiber pull-out, and fiber bridging can all be measured and related to micromechanical properties. Results here show that when we account for matrix cracking below the resolution of the CT images, between 35 and 48% of the internal energy dissipation in the tested fiber reinforced concrete can be attributed to the fracture energy of the cement-based matrix. The work of fiber pull-out represents between 28 and 34%, while fiber bridging (an indirect form of fiber pull-out) accounted for between 7 and 25%. Fiber bending was negligible at 1 to 2%. For the specimens tested, these mechanisms added up to between 89 and 93% of the total inelastic energy consumed in the loaded specimen. We suggest the unaccounted for energy, nominally 10%, could be attributed to creep deformations, localized damage at the supports, and other mechanisms that either do not manifest themselves in the form of measurable changes in microstructure or are beyond the resolution of the images. While limitations exist in the measurements, the work does provide a rational starting point for how toughening mechanisms can be isolated.

**Table 4:** Internal Energy Dissipation Totals Revised to Included Additional Matrix Cracking

	Energy of Matrix Cracking ( $W_f$ )	Work of Fiber Pullout ( $W_p$ )	Work of Fiber Bending ( $W_b$ )	Work of Fiber Bridging ( $W_r$ )	Total Internal Energy Dissipated ( $E_{int}$ )	Fraction Internal to External ( $U_{int}/U_{ext}$ )
	mJ (% of $E_{int}$ )				mJ	%
Beam 4	2500 (35)	2020 (28)	130 (2)	1950 (26)	6600	90
Beam 5	7000 (48)	4720 (32)	190 (1)	1000 (7)	12910	89
Beam 6	4400 (38)	3890 (34)	180 (2)	2270 (20)	10760	93

## 7 Acknowledgements

This work was conducted under Contract W912HZ-09-C-0059 from the Engineer Research and Development Center (ERDC) of the U.S. Army Corps of Engineers.

## REFERENCES

- [1] Bentur, A. and Mindess, S., 1990. *Fiber Reinforced Cementitious Composites*. Elsevier Science.
- [2] Balaguru, P.N. and Shah, S.P., 1992. *Fiber-reinforced cement composites*. McGraw-Hill Companies.
- [3] Bonneau, O. and Poulin, C. and Dugat, J. and Richard, P. and Aitcin, P.C. 1996. Reactive powder concrete: from theory to practice. *Concrete International* **18**:47–49.
- [4] Williams, E.M., Graham, S.S., Reed, P.A. and Rushing, T.S. 2009. *Laboratory Characterization of Cor-Tuf Concrete With and Without Steel Fibers*. U.S. Army Engineer Research and Development Center.
- [5] Martz H.E., Schneberk, D.J., Robertson, P.G., and Monteiro, P.J.M. 1993. Computerized Tomography of Reinforced Concrete. *ACI Materials Journal* **90**:259–264.
- [6] Landis, E.N., Zhang, T., Nagy, E.N., Nagy, G., and Franklin, W.R. 2007. Cracking, damage and fracture in four dimensions. *Materials and Structures* **40**:357–364.
- [7] Krause, M., Hausherr J.M., Burgeth, B., Herrmann C., and Krenkel W. 2009. Determination of the fibre orientation in composites using the structure tensor and local X-ray transform. *Journal of Materials Science* **45**:888–896.
- [8] Lorenz, C., Carlson, I.-C., Buzug, T.M., Fassnacht, C., and Weese, J. 1997. Multi-scale line segmentation with automatic estimation of width, contrast and tangential direction in 2D and 3D medical images. In *First Joint Conference on Computer Vision, Virtual Reality and Robotics in Medicine, and Medical Robotics and Computer-Assisted Surgery*. Springer. pp. 233–242.
- [9] Nagel, H.-H. 2006. On the Concept of a Local Greyvalue Distribution and the Adaptive Estimation of a Structure Tensor. in J. Weikert and H. Hagen (eds), *Visualization and Processing of Tensor Fields*. Springer-Verlag.
- [10] Rushing, T.S. 2010. unpublished data.
- [11] Shah, S.P. 1992. Do Fibers Increase the Tensile Strength of Cement-Based Matrix?. *ACI Materials Journal* **88**:595-602.